Small-scale gravitational instabilities under the oceans: Implications for the evolution of oceanic lithosphere and its expression in geophysical observables

S. Zlotnik[a]*, J.C. Afonso[a], P. Díez[b] and M. Fernández[a]

[a]*Group of Dynamic Lithosphere (GDL), Earth Sciences Institute "Jaume Almera", CSIC, Barcelona, Spain;* [b]*Laboratori de Calcul Numeric (LaCAN), Universitat Politecnica de Catalunya (UPC), Barcelona, Spain*

Sublithospheric small-scale convection (SSC) is thought to be responsible for the flattening of the seafloor depth and surface heat flow observed in mature plates. Although the existence of SSC is generally accepted, its ability to effectively produce a constant lithospheric thickness (i.e. flattening of observables) is a matter of debate. Here we study the development and evolution of SSC with a 2D thermomechanical finite-element code. Emphasis is put on (i) the influence of various rheological and thermophysical parameters on SSC, and (ii) its ability to reproduce geophysical observables (i.e. seafloor depth, surface heat flow, and seismic velocities). We find that shear heating plays no significant role either in the onset of SSC or in reducing the lithospheric thickness. In contrast, radiogenic heat sources and adiabatic heating exert a major control on both the vigour of SSC and the thermal structure of the lithosphere. We find that either dislocation creep, diffusion creep, or a combination of these mechanisms, can generate SSC with rheological parameters given by laboratory experiments. However, vigorous SSC and significant lithospheric erosion are only possible for relatively low activation energies. Well-developed SSC occurs only if the first $\sim$300 km of the mantle has an average viscosity of $\lesssim 10^{20}$ Pa s; higher values suppress SSC, while lower values generate unrealistic high velocities. Seismic structures predicted by our models resemble closely tomography studies in oceanic mantle. However, the fitting to observed seafloor topography and surface heat flow is still unsatisfactory. This puts forward a fundamental dichotomy between the two datasets. This can be reconciled if most of the observed flattening in seafloor topography is influenced by processes other than SSC.

Keywords: small scale convection; oceanic lithosphere; rheology; lithosphere evolution; numerical methods

1. Introduction

Oceanic lithosphere is being continuously created at mid-ocean ridges, where adjacent plates move apart from each other in a process called seafloor spreading [1]. As these plates diverge, hot mantle rocks ascend to fill the gap. Upon subsequent conductive cooling, these rocks become rigid and form new oceanic lithosphere. The complementary

*Corresponding author. Email: szlotnik@ija.csic.es

process of plate consumption occurs along subduction zones, where plates bend and descend into the Earth's mantle. The entire process of creation, lateral displacement, and eventual subduction of oceanic lithosphere can be thought of as a large-scale convection cell, where the oceanic lithosphere represents the upper thermal boundary layer.

As oceanic plates move away from ridges, they cool from above, thicken, and become denser by thermal contraction. This cooling is reflected on the dependence of geophysical observables on the age of the plate t [2,3]. For plates younger than about 70 My, both seafloor topography and surface heat flow (SHF) decrease linearly as $\sqrt{t}$, consistent with predictions from the *half-space cooling model* [4].

For larger ages, however, this relation breaks down and the two observables decrease less rapidly, reaching almost constant values in ocean basins [3,5,6]. Since these observables reflect the thermal structure of the lithosphere, their flattening implies a similar behaviour for the isotherms within the plate. These features are included in the popular *plate model* [2], which considers the lithosphere as a cooling plate with an isothermal lower boundary. Although this model can explain the observed flattening of both seafloor topography and SHF, it does not propose any particular mechanism by which the horizontal isotherm is maintained at constant depth.

One such mechanism, known as small-scale convection (SSC) [7], involves the generation of thermal instabilities at the lower parts of the lithosphere. Conductive cooling causes the isotherms to migrate downwards until the cold material at the base of the lithosphere becomes gravitationally unstable and SSC is triggered. This mechanism provides the necessary extra heat to keep a horizontal and isothermal lithospheric base, by replacing cold (dense) material with hotter mantle. The resulting thermal erosion would maintain a quasi-constant lithospheric thickness through time.

Small-scale convection has been studied using theoretical (e.g. [7–9]), numerical (e.g. [10–16]) and analogue models (e.g. [17]). These studies have been focused on the general conditions for the existence of SSC, but none attempted a systematic exploration of the effects of all relevant physical parameters on SSC. Moreover, either seismically derived thermal structures or SHF and seafloor topography data have been used to test the reliability of the results, but no study has combined these three observables into a single consistent model. This is of particular relevance, because seismic observations seem to favour half-space cooling models over plate models, while SHF and seafloor topography observations suggest the opposite.

This work presents a systematic study of the influence of several rheological and thermophysical parameters on SSC, its expression in geophysical observables, and its role in determining the thickness of oceanic lithosphere. Predictions of seismic velocities, SHF and seafloor topography are used to ensure compatibility with current observations. In the following sections we first introduce the statement of the problem and the applied numerical methods; we then describe the approach to calculate the relevant geophysical observables; finally, we discuss the results and their implications on the evolution of the oceanic lithosphere.

2. Model description

2.1. *Governing equations*

The Earth's mantle behaves as a highly viscous fluid over the long time-scale ($t > 10^4$ yr) (cf. [1,18]). Since the physical properties of this fluid are strongly dependent on

temperature, the physical model involves a mechanical flow problem coupled to a thermal problem. We consider an incompressible fluid in a rectangular domain. Due to the almost infinite Prandtl number of the fluid, inertial terms are neglected and the problem becomes quasi-static. The transient character of the solution is due to the evolution of the temperature field. Under the Boussinesq approximation (i.e. the effects of density variations other than in the body-force terms are neglected), the three unknowns, velocity $\mathbf{u}$, the pressure P and the temperature T are determined by solving the conservation of momentum (Stokes equation), mass, and energy equations (cf. [1]):

$$\nabla \cdot (\eta \nabla^{\mathrm{s}} \mathbf{u}) + \nabla P = \rho \mathbf{g} \tag{1}$$

$$\nabla \cdot \mathbf{u} = 0 \tag{2}$$

$$\rho C_p \left(\frac{\partial T}{\partial t} + \mathbf{u} \nabla T \right) = \nabla \cdot (k \nabla T) + \rho f, \tag{3}$$

where the operator ∇^{s} is the symmetrised gradient, namely $1/2(\nabla^{\top} + \nabla)$, η is the viscosity, ρ the density, $\mathbf{g}$ the gravitational acceleration vector, C_p the isobaric heat capacity, k the thermal conductivity, and f a heat source term which is the sum of: (i) a constant term f_r corresponding to the decay of radioactive elements, (ii) an adiabatic heating term $f_{\mathrm{ah}} \approx T\alpha\rho u_z g_z$, where α denotes the coefficient of thermal expansion and subscript z refers to the vertical component of the vectors, and (iii) a shear heating term associated with mechanical heat dissipation. The shear heating is computed from Equations (1) and (2) as $f_{\mathrm{sh}} = \sigma_{ij}\dot{\varepsilon}_{ij}$, where σ and $\dot{\varepsilon} = \nabla^{\mathrm{s}}\mathbf{u}$ are the stress and strain rate tensors. As the constitutive equation described in the next section depends on the velocity, the system is highly non-linear.

The mechanical problem (Equations (1) and (2)) is solved in an Eulerian framework with the finite element method using a mixed formulation in terms of velocity and pressure. We use the well-known triangular mini element ($\mathrm{P1}^{+}$-P1) [19], with four nodes for the velocity (three at the vertices with linear shape functions and one at the centre with a cubic bubble function) and three pressure nodes (piecewise linear interpolation). The mini element exhibits linear convergence. It has been reported [19] that the accuracy of pressure approximations provided by the mini element is degraded in 3D with respect to the more accurate and computationally demanding Taylor-Hood element (P2-P1). Nevertheless, in the 2D examples presented in this paper, the pressure is almost linear and it is fairly approximated using the mini element with a minimum computational cost.

A basic Picard method is used to handle the non-linear character introduced by the constitutive equation. In most cases, this simple method converges to the desired accuracy in a reduced number of iterations. Due to the quasi-static character of the mechanical model, the time evolution is determined solving a series of steady state problems. On the other hand, the thermal model (Equation (3)), has to be integrated over time using a time stepping strategy. This requires a space–time discretisation. The space discretisation is performed using standard linear finite elements with a Galerkin formulation, while the time discretisation uses an explicit fourth-order Padé method [19], which properly accounts for both the advective and the diffusive part of the equation. The explicit nature of the time stepping scheme used for the thermal model, together with the quasi-static character of the mechanical problem, allows us to solve the thermo-mechanical coupling

using a staggered scheme. The explicit scheme for the thermal problem is conditionally stable. The time step must be sufficiently small to fulfil the stability requirements established by limiting the Courant number. This small time step guarantees the stability of the thermal scheme and, hence, of the fully coupled thermo-mechanical model.

The models we are using consider only one type of material (with characteristics associated with the mantle; the oceanic crust is not included in the modeling). Moreover, all physical properties (viscosity, thermal conductivity, density, etc.) are computed as explicit functions of T, P, $\mathbf{u}$. Consequently, there is no need for tracking the Lagrangian motion of the material. The reader is referred to [20] for examples of Lagrangian tracking of different materials using a level-set approach.

Non-linearity in Equation (3) arises due to the dependency of density and thermal conductivity on temperature. It is assumed that within a time step the material properties (ρ and k) can be approximated by their values at the beginning of the time step. This simplifies the implementation and reduces the computational cost. A detailed description of the numerical strategy used here to solve the thermo-mechanical coupled problem is given in [20].

2.2. *Constitutive equation*

Convective flow in the Earth's mantle is possibly due to the high-temperature creep of mantle rocks. This solid-state deformation mechanism occurs due to the thermally activated motion of atoms associated with lattice defects such as dislocations and vacancies (cf. [21]). There is general agreement that two main creep mechanism are likely responsible for most of the deformation in the mantle: diffusion creep (Herring-Nabarro and Coble creep) and dislocation creep [21,22]. Although there are significant uncertainties associated with the extrapolation of laboratory results (performed at low pressures and high strains rates) to mantle conditions, a comparison of microstructures on experimentally and naturally deformed peridotites indicates that the same deformation mechanisms detected in the laboratory take place in the mantle as well [21,23]. Deformation caused by dislocation creep is evidenced in lithospheric mantle samples (e.g. xenoliths, peridotitic massifs) and indirectly inferred in the shallow upper mantle from seismic anisotropy studies (see [24] for a recent review). On the other hand, diffusion creep may be dominant over dislocation creep at depths >250–300 km, where stresses are low and pressure effects become dominant (i.e. the activation volume of diffusion creep seems to be smaller than that of dislocation creep [21]). This change in deformation mechanism with depth is consistent with the lack of significant anisotropy at such depths, although not conclusive [25].

Theoretical treatments and experimental observations demonstrate that the macroscopic creep behaviour of rocks is well described using a 'power-law' of the form [21,26,27]

$$\dot{\varepsilon} = A(\sigma'/\mu)^n (b/d)^m \exp\left(-\frac{E+PV}{RT}\right), \tag{4}$$

where d is the average grain-size, σ' the deviatoric stress, A the pre-exponential factor, μ the shear modulus, b the length of the Burgers vector, n the stress exponent, m the grain-size exponent, E the activation energy, V the activation volume, and R the gas

constant (see Table 4). The combination of Equation (4) with the definition of viscosity ($\eta = \frac{1}{2}\sigma'/\dot{\varepsilon}$), allows isolating an explicit expression for η in terms of T, P and $\dot{\varepsilon}$. This expression is then used to solve Equation (1).

To compute the viscosity, we assume a constant material parameter $A_D = \frac{1}{2} A^{-1/n}\mu^{-1}(b/d)^{-m/n}$, including the pre-exponential factor A, the grain-size dependence, and the shear modulus. Although grain-size may change due to grain growth and dynamic recrystallisation processes, its dependence on stress is not well known. We simplify the rheology here by assuming a constant grain size.

Diffusion and dislocation creep act simultaneously in the mantle [21]. In order to account for the effect of the two mechanisms, two different viscosities η_{diff} and η_{disl} are computed separately and then combined into an effective viscosity η_{eff}, which is computed as the harmonic mean of η_{diff} and η_{disl}:

$$\frac{1}{\eta_{\text{eff}}} = \left(\frac{1}{\eta_{\text{diff}}} + \frac{1}{\eta_{\text{disl}}}\right). \tag{5}$$

This expression is truncated if the resulting viscosity is either greater or lower than two imposed cutoff values (10^{18} to 10^{24} Pa s). The viscosity η_{diff} is computed using $n = 1$, while for η_{disl} we use $m = 0$. The values of the rest of the parameters are described Section 3.

2.3. *Phase transitions and mineral domains*

At least four main solid–solid mineral phase transitions occur in the mantle region considered in this study: plagioclase-spinel, spinel-garnet, olivine-wadsleyite, and wadsleyite-ringwoodite. Other phase transitions (e.g. orthoenstatite to clinoenstatite) may occur within the domain, but their effect on the type of gravitational instabilities of interest is negligible. Here we consider explicitly only the olivine-wadsleyite, and wadslayite-ringwoodite phase changes, which are the most relevant in terms of density and viscosity contrasts that may exert a control on the vertical structure of SSC. Each of these phase transitions is characterised by a particular Clapeyron slope, which we approximate as linear functions in the temperature-pressure domain (see Table 1). The olivine-wadsleyite and wadsleite-ringwoodite transitions occur at ~410 and 510 km depth, respectively, in a pyrolitic adiabatic mantle. In the oceanic mantle, the plagioclase-spinel and spinel-garnet transitions occur at depths of ~30 and 50–80 km, respectively [28]. The depth variability in the latter is due to the exothermic nature of the reaction and the rapid horizontal temperature variation in the shallow oceanic upper mantle. In principle, the spinel-garnet phase change occurs deep enough to be affected by SSC,

Table 1. Phase transition parameters.

Depth(km)	Slope(MPa K^{-1})	T(K)	P(MPa)	$\Delta\rho$ (kg m^{-3})
410[a]	4.0	1600	14,200	250
510[b]	4.0	1700	17,000	0
660[c]	−2.5	1873	23,100	250

[a] from [29], [b] from [30], [c] from [31].

and given its exothermic nature and associated density change (0.8–1.0%, [28]), it could promote SSC through buoyancy enhancement (cf. [1]). However, the present study is focused on the role that other major physical parameters play on the development of SSC, and therefore we leave petrological and phase change effects for a future study (work in progress).

Representative reference properties for the whole mantle are estimated, considering the stable phases at different temperatures and pressures. Therefore, the average rock properties are computed as follow: (i) the volumetric fractions of the major constituent phases along a 1600 K adiabat are taken from [32] (see Table 2), (ii) each phase is identified with only one (the most abundant) end-member (e.g. enstatite for opx, diopside for cpx, pyrope for grt), (iii) experimentally derived properties of these end-members are taken from the references listed in Tables 1–3, and finally (iv) the average rock properties are computed as either the arithmetic mean of the end-members weighted by their respective volumetric proportions or with a Voigt-Reuss-Hill averaging scheme. The latter is used only when calculating the elastic moduli for seismic velocities. We acknowledge that this approach is only valid to the first-order and lacks thermodynamic consistency. However, it gives values comparable, within one standard deviation, to those obtained with more sophisticated methods (e.g. [32,33]) with a minimum of computational time.

Table 2. Stable phases at different depths. After [32].

Mineral	200 km	420 km	600 km	800 km
Olivine (Fo)	51.3%	0	0	0
Olivine (Fa)	5.7%	0	0	0
Orthopyroxene (Enstatite)	13.5%	0	0	0
Clinopyroxene (Diopside)	10.0%	0	0	0
Garnet (Pyrope)	19.6%	40.0%	37.5%	0
Wadsleyite	0	60.0%	0	0
Ringwoodite	0	0	60.0%	0
Ferropericlase	0	0	0	16.0%
Mg perovskite	0	0	0	78.0%
Ca perovskite	0	0	2.5%	6.0%

Table 3. Parameters for thermal expansivity α.

Param.	200 km	420 km	600 km
$a_0(\times 10^{-5})$	2.65032	2.43507	2.30551
$a_1(\times 10^{-9})$	9.19917	2.97727	2.79119
a_2	−0.27127735	−0.184206667	−0.17269375
a_3	0	0	0

Parameters for the different phases were taken from: forsterite, fayalite, enstatite, diopside, pyrope: [28]; wadsleyite, ringwoodite: [35]; ferropericlase, Ca-perovskite: [36]; Mg-perovskite: [37].

Coefficient of thermal expansion. The thermal dependence of the coefficient of thermal expansion at pressure P_0 is approximated by a polynomial expression of the form (e.g. [28,34])

$$\alpha(P_0, T) = a_0 + a_1 T + a_2 T^{-2} + a_3 T^4. \tag{6}$$

The averaged coefficients for each stability field are listed in Table 3.

The pressure effect on the coefficient of thermal expansion can be described by the Anderson-Grüneisen parameter δ [38,39] as

$$\alpha(P, T) = \alpha(P_0, T)\left(\frac{\rho(P, T)}{\rho(P_0, T)}\right)^{\delta\frac{\rho(P_0, T)}{\rho(P, T)}} \approx \alpha(P_0, T)(1 + \beta(P - P_0))^{\delta(1+\beta(P-P_0))}. \tag{7}$$

The approximation in Equation (7) provides an explicit formula to compute the thermal expansion coefficient in terms of pressure and temperature.

Density. Density changes associated with temperature and pressure variations accompanying convection are small compared to the spherically averaged density of the mantle. Therefore, it is appropriate to simplify the density ρ as a linear function of temperature and pressure with respect to a reference value ρ_0 (calculated in a previous step as described above). Our simplified equation of state is of the form

$$\rho(P, T) = \rho_0\big[1 - \alpha(P, T) \times (T - T_0)\big] \times \big[1 + \beta \times (P - P_0)\big], \tag{8}$$

where β is the compressibility, and T_0 and P_0 are, respectively, the temperature and pressure at which the reference density ρ_0 is given.

Thermal conductivity. The thermal conductivity is calculated using the model of [40], which gives the relation,

$$k(P, T) = k_{298}\left(\frac{298}{T}\right)^a \exp\left[-\left(4\gamma + \frac{1}{3}\right)\int_{298}^{T} \alpha(\theta)\,\mathrm{d}\theta\right]\left(1 + \frac{K'_0 P}{K_0}\right) + k_{\mathrm{rad}}, \tag{9}$$

where k_{298} is the thermal conductivity measured at ambient conditions, a is a parameter with a value $\sim$0.33 for silicates, γ the averaged thermal Grüneisen parameter, K_0 is the isothermal bulk modulus, and K'_0 its pressure derivative. The last term k_{rad} is the radiative contribution, approximated by the polynomial function

$$k_{\mathrm{rad}} = b_0 + b_1\, T + b_2\, T^2 + b_3\, T^3, \tag{10}$$

where temperature T is in kelvin. Refer to Table 4 for a list of representative parameters.

2.4. *Geophysical constraints to mantle dynamics*

Geophysical observables are commonly used to infer the physical state of the Earth's interior. Available datasets that help to constrain, to different extents, mantle dynamics include ocean floor topography, surface heat flux, seismic velocities, and gravity. As a post-process of our simulations, we estimate these observables [41].

Table 4. Physical and geometrical model parameters.

Symbol	Meaning	Value used	Dimension
H	model height	660	km
W	model width	7000 or 10,000	km
$\mathbf{g}$	gravity acceleration vector	[0, −9.8]	$\mathrm{m\ s^{-1}}$
R	gas constant	8.314510	$\mathrm{J\,mol^{-1}\,K^{-1}}$
T_0	reference temperature	273	K
p_0	reference pressure	0.1	MPa
ρ_{ol}	reference density	3300	$\mathrm{kg\ m^{-3}}$
β	compressibility coefficient	1×10^{-5}	$\mathrm{MPa^{-1}}$
C_p	thermal capacity	1200	$\mathrm{J\ kg^{-1}\,K^{-1}}$
f_r	radiogenic heat production	2×10^{-8}	$\mathrm{W\ m^{-1}\,K^{-1}}$
μ	shear modulus	80	GPa
b	length of the Burgers vector	0.5	nm
γ	Grüneisen parameter	1.28	
δ	Anderson-Grüneisen parameter	5.5	
K_0	bulk modulus	120	GPa
K'_0	K_0 derivative with respect to pressure	4.5	
$b_0/b_1/b_2/b_3$	radiation polynomial approx.	$0/0/0/8.5\times10^{-11}$	

Seafloor topography. Seafloor topography is estimated assuming local isostasy (i.e. mass per unit area of a vertical column is compared with respect to a reference value taken at the ridge). Following [42], we define the isostatic topography w_{iso} as

$$w_{\mathrm{iso}} = \int_0^{d_{\mathrm{com}}} (\rho - \rho_{\mathrm{ref}})\,\mathrm{d}z, \tag{11}$$

where d_{com} is a compensation depth, and ρ_{ref} the density of a reference column. Although the choice of d_{com} is somewhat arbitrary, it should be taken close to the depth of the deepest isotherm with a dominant conductive component. Isotherms significantly deflected by convection are associated with dynamic loads that are not isostatically compensated (see dynamic topography below).

Dynamic topography. Vertical components of mantle flow may result in a modification of the surface topography. The resulting topography arising from this mechanism is known as *dynamic topography*, to distinguish it from that part of the topography resulting from the isostatic compensation of *static* loads (see above). Following [43], we estimate the dynamic component of topography w_{dyn} as

$$w_{\mathrm{dyn}} = \frac{\sigma_{zz}}{\rho\, g}, \tag{12}$$

where σ_{zz} is the vertical stress component acting on the surface, ρ the density, and g the vertical component of the gravity acceleration. Convective shear stresses acting at the base of the lithosphere would also have an effect in the dynamic topography. However, they typically represent less than 5% of the dynamic topography generated by vertical stresses and therefore they can be neglected [44]. In all our simulations the dynamic topography associated with SSC never exceeds ±150 m. This number would be reduced by as much as 75% if we included the elastic strength of the plate [44].

Table 5. Solution notation and formulae.

Symbol	Meaning	Value used
Ol	olivine	$[Mg_xFe_{1-x}]_2SiO_4$
Opx	orthopyroxene	$[Mg_xFe_{1-x}]_{2-y}Al_{2y}Si_{2-y}O_6$
Sp	spinel	$Mg_xFe_{1-x}Al_2O_4$
Cpx	clinopyroxene	$Ca_{1-y}[Mg_xFe_{1-x}]_{1+y}Si_2O_6$
Gt	garnet	$Fe_{3x}Ca_{3y}Mg_{3(1-x+y+z/3)}Al_{2-2z}Si_{3+z}O_{12}$; $x+y+4z/3 \leq 1$
C2/c	pyroxene	$[Mg_xFe_{1-x}]_4Si_4O_{12}$
Aki	akimotoite	$Mg_xFe_{1-x-y}Al_{2y}Si_{1-y}O_3$, $x+y \leq 1$
Pv	perovskite	$Mg_xFe_{1-x-y}Al_{2y}Si_{1-y}O_3$, $x+y \leq 1$
Ppv	post−perovskite	$Mg_xFe_{1-x-y}Al_{2y}Si_{1-y}O_3$, $x+y \leq 1$
Ring	ringwoodite	$[Mg_xFe_{1-x}]_2SiO_4$
Wad	waddsleyite	$[Mg_xFe_{1-x}]_2SiO_4$
Wus	magnesiowuestite	$Mg_xFe_{1-x}O$

Unless otherwise noted, the compositional variables x, y, and z may vary between zero and unity and are determined as a function of the computational variables by free-energy minimisation.

Seismic velocities. The calculation of seismic velocities [$V_p^2\rho = K_S + 4/3G$ and $V_s^2\rho = G$] requires knowing the elastic moduli of each stable phase, the density of the bulk rock at the pressures and temperatures of interest, and estimations of anelastic attenuation. Here we compute these properties by a free energy minimisation procedure (see details in [45]) within the system CFMAS (CaO-FeO-MgO-Al_2O_3-SiO_2). These five major oxides make up more than 98% of the Earth's mantle, and therefore, they constitute an excellent representation of mantle's composition. The minimisation program (PerpleX) requires a thermodynamic database for pure end-members and solution models to compute the properties of stable phases (usually solid solutions of two or more end-members). The thermodynamic database used in the energy-minimisation is that of [32] with solution models as listed in Table 5.

The thermal and pressure fields necessary to calculate the seismic velocities are obtained from the thermo-mechanical simulation. This generates an unavoidable inconsistency between the density values used to calculate buoyancy forces in the thermo-mechanical problem and those used to calculate seismic properties in the energy-minimisation scheme (densities from the energy-minimisation are systematically greater than those from the thermo-mechanical simulation). Parallel computations indicate that this inconsistency translates into errors of $\lesssim$1.1% in our calculated *absolute* seismic velocities. However, the seismic structure (i.e. spatial velocity distribution) generated by our models is not significantly affected.

Anelastic effects are computed as a function of grain size (d), oscillation period (T_o), T, P, and empirical parameters A, E, and α as [41,46]

$$V_\theta = V_{\theta_o}(P,T)\left[1 - \zeta \cot\left(\frac{\pi\alpha}{2}\right) Q_s^{-1}(T_o, T, P, d)\right], \tag{13}$$

where $V_{\theta_o}(P,T)$ is the unrelaxed high frequency wave velocities at a given temperature and pressure (i.e. including anharmonic effects) and θ stands for either P-wave or

S-wave velocities. The term ζ takes the values 2/9 and 1/2 for P-waves and S-waves, respectively [41]. The quality factor is represented as

$$Q_s^{-1}(T_o, T, P, d) = A\left[T_o\, d^{-1} \exp\left(\frac{-E + VP}{RT}\right)\right]^{\alpha}, \tag{14}$$

with $A = 750\ \mathrm{s}^{-\alpha}\,\mu\mathrm{m}^{\alpha}$, $\alpha = 0.26$, $E = 424\,\mathrm{kJ\,mol}^{-1}$, $V = 1.2\text{-}1.4\times10^{-5}\,\mathrm{m}^3\,\mathrm{mol}^{-1}$, and R the universal gas constant [47,48].

2.5. *Model setup and boundary conditions*

The simulation domain is a rectangular box, representing a vertical plane parallel to the plate motion (Figure 1). The box is divided into approximately 13,000 triangular elements, representing a vertical thickness of 660 km in nature. The horizontal dimension is 7000 or 15,000 km wide, depending on the particular model. Since the oceanic crust does not play any significant role on the dynamics of SSC, it is neglected in our model. Temperature boundary conditions assume constant temperatures at the surface and at the bottom of the simulation domain. The initial internal temperature distribution follows the half-space cooling model, which is calculated in terms of the surface temperature T_{surf}, temperature at the bottom of the lithosphere T_{lith}, and thermal diffusivity κ as [1]

$$T(t, z) = (T_{\mathrm{surf}} - T_{\mathrm{lith}})\ \mathrm{erfc}\left(\frac{z}{2\sqrt{\kappa\, t}}\right) + T_{\mathrm{lith}}, \tag{15}$$

where t is the age of the plate, z is the depth, and erfc is the complementary error function. The age t is directly related to the horizontal space dimension through the plate velocity. This model gives 'conductive' temperatures above a specific isotherm T_{lith}, which represents the base of the lithosphere. For temperatures below this isotherm, a linear interpolation is done between T_{lith} (here chosen = 1603 K) and the temperature at the bottom of the box, T_{bot}. The latter is chosen to be 1880 K, in accordance with results from high-pressure and high-temperature experiments on mineral phase equilibria (e.g. [29]). On the laterals the normal flow is set to zero.

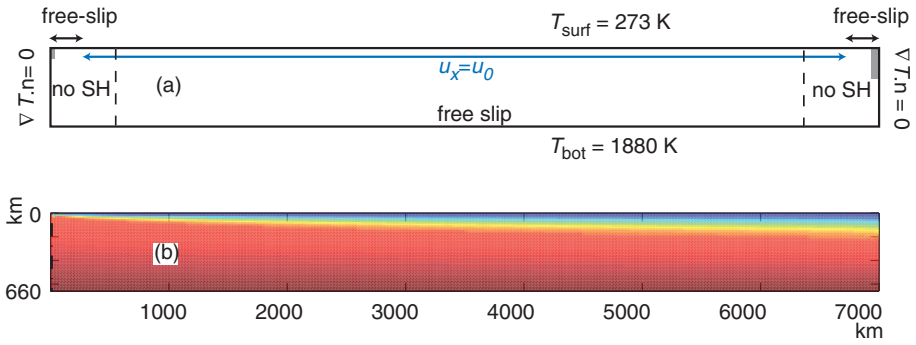

Figure 1. (Colour online). Boundary (a) and initial (b) conditions for SSC models. The grey areas in panel (a) are the regions were viscosity is decreased. The dashed lines delimit areas where shear heating is neglected.

The initial velocity field is set to zero in the entire domain. A constant horizontal velocity is imposed at the top of the model, everywhere but near the corners (see Figure 1a). The vertical velocity at the top of the box is zero. Imposing a constant velocity at the top along the entire domain length, generates singularities in the upper corners (and nearby regions) where the strain rate reaches unrealistic high values and consequently high shear heating. We emphasise that these extremely high strain rate values are numerical artifacts produced by the boundary conditions, and consequently they do not represent any relevant physical process. To avoid these undesired effects we use a free-slip condition in regions near both corners, which leads to the generation of a smoother corner flow. For similar reasons, we further introduce two small weak zones near the upper corners (see Figure 1a), as commonly done in similar studies [12]. The viscosity in these regions is divided by 10, 100 or 1000 depending on the model. In the other three sides of the domain, free-slip boundary conditions are imposed. To avoid excessive heating generation at the corners of the model, shear heating is turned off within two rectangular areas at the ends of the domain (see Figure 1a). Each rectangle represents 10% of the total domain length. Since we are interested in the generation and evolution of SSC regions well outside these regions, the neglect of shear heating within them does not affect our results and conclusions.

No initial condition needs to be specified for the pressure. This is a consequence of the fact that no time derivative of pressure appears in the governing equations (Equations (1)–(3)). When velocity is imposed everywhere on the boundaries, only pressure gradients appear in Equation (1), and total pressure can be determined by assuming an arbitrary constant (usually $P=0$) at some 'quiescent' point at the surface.

3. Results

We organise this section in two parts. In the first part we describe the main features of SSC and its effect on the thermal structure of both the lithosphere and sublithospheric mantle. In the second part, we systematically analyse the influence of key physical parameters on the generation and evolution of SSC.

3.1. *General features of small-scale convection*

In this section, we present an illustrative model in which SSC is fully developed. The imposed upper velocity is $3.5\,\mathrm{cm\ yr^{-1}}$, comparable to absolute velocities reported for oceanic plates [49]. The only internal heating term included in the energy equation is the adiabatic heating (i.e. shear heating and radiogenic heat production are set $=0$). The model assumes a Newtonian rheology with the following parameters: activation energy $E=120\,\mathrm{kJ\,mol^{-1}}$, activation volume $V=4\times10^{-6}\,\mathrm{m^3\,mol^{-1}}$, and pre-exponential factor $A_D=7.6\times10^{-16}\,\mathrm{Pa^{-n}\ s^{-1}}$. Similar values have been extensively used in earlier studies on SSC (e.g. [11–14]), allowing qualitative comparisons between these and our models. We emphasise, however, that these activation energy and pre-exponential factor values are too low to be consistent with currently available laboratory experiments on diffusion creep (e.g. [23,26]). A complete discussion on the effects of these parameters on the development and evolution of SSC is provided in the next section.

Figure 2a shows the resulting thermal structure after 83 My of simulation time (*simulation time* is the total number of time-steps in My, and should not be confused with *plate age*, t, which is related to the horizontal dimension D and the imposed velocity v as $t = D/v$). At this time, the model is already in a 'dynamic steady-state'. During this stage, the onset of SSC occurs at ~2100 km from the ridge (dotted line in Figure 2), or what is the same, when the lithosphere is ~60 My old. We note that neither lateral boundary conditions nor the downstream developed at the rightmost part of the model (not shown in Figure 2), influence these SSC instabilities. At shorter distances (younger lithosphere), the isotherms follow closely the initial thermal structure predicted by the half-space cooling model. The wavelength of the instabilities is of the order of 150–200 km throughout the entire model. Some isotherms (in kelvin) are plotted to show the perturbing effect of SSC. The 1603 K isotherm, which is typically

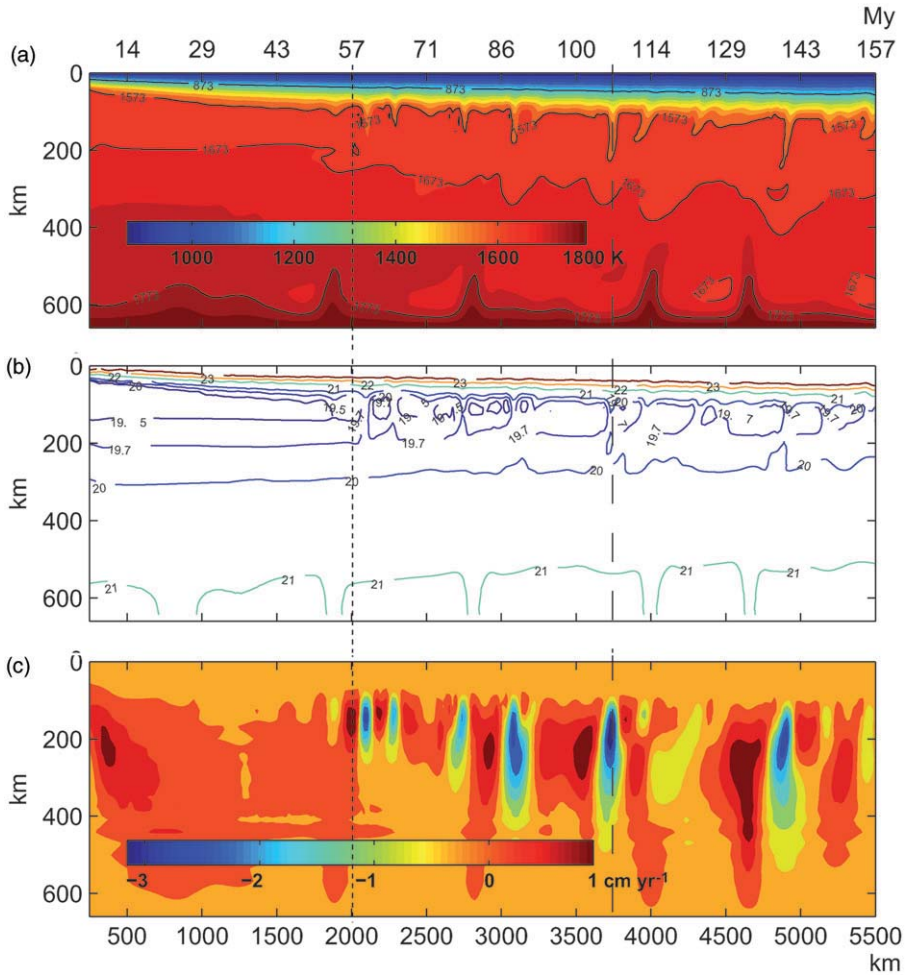

Figure 2. Typical temperature (a), viscosity (b) and vertical velocity (c) when small-scale convection develops. See text for details.

assumed to represent the base of the lithosphere, is completely distorted due to SSC (advection-dominated). Even the 1473 K isotherm shows an advective component, although considerably less than hotter isotherms.

The resulting viscosity structure is plotted in Figure 2b. In order for SSC to develop, we find that the viscosity of the upper 300 km of mantle needs to remain lower than 10^{20} Pa s. Higher values suppress SSC, while lower values generates unrealistic high velocities. We will discuss further the effects of viscosity in the next section. Here we only note that the above value is similar to those previously reported by different authors [12,13,50]. Figure 2c shows the vertical component of the velocity vector. Small-scale convection produces a significant vertical flow. Maximum velocities reach values of about 6 cm yr^{-1}, which is a factor of two greater than the imposed surface velocity. Strain rate values are within the range of 10^{-14}–10^{-15} s^{-1}, between 100 and 500 km depth; the greatest values in the entire domain are always associated with SSC cells.

As expected, SSC slows down the conductive cooling of the lithosphere by replacing cold mantle with hotter mantle, effectively reducing its thermal thickness when compared with predictions from the half-space cooling model. Likewise, the underlying sublithospheric mantle is cooled by the cold downwellings. We illustrate this effect in Figure 3. This figure compares temperature profiles across the mantle at different simulation times, starting from the initial temperature distribution given by the half-space cooling

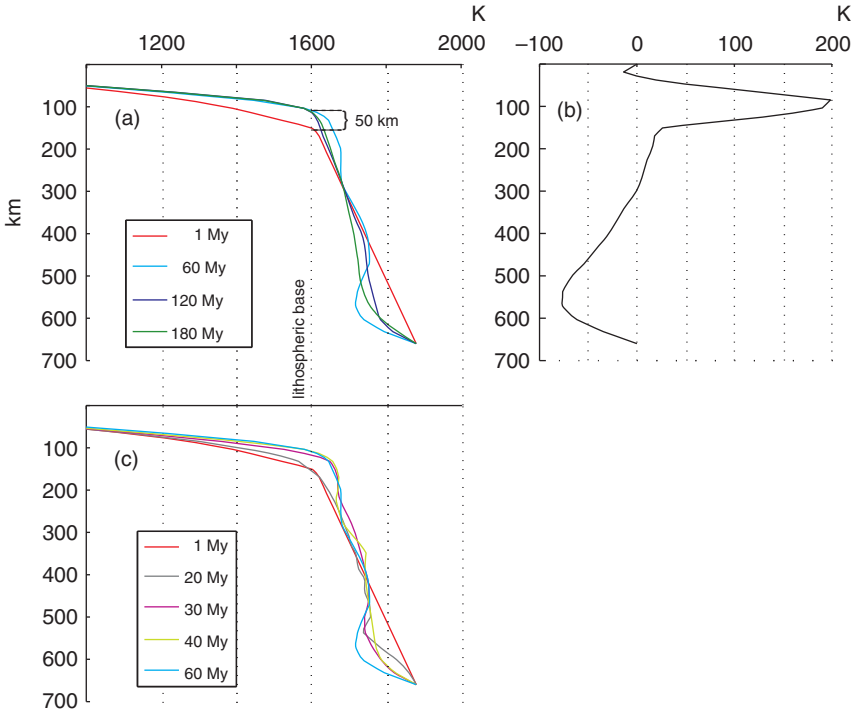

Figure 3. (Colour online). Temporal evolution of temperature for model 16 at 3000 km away from ridge. Panel (a) and (c): temperature profiles at different times. Panel (b) temperature variation between 1 and 180 My.

model (1 My in Figure 3, red line online). The profiles are located at 3000 km away from the ridge, where the plate is 85.7 My old. To remove short-wavelength temperature anomalies, the temperature is horizontally averaged in a 400 km region (from $x = 2800$ to 3200 km). The profiles in Figure 3a, clearly show that the lithosphere reaches a 'steady' thermal thickness after ~60 My of simulation time. However, a closer inspection (Figure 3c) reveals that this steady thickness is reached after only ~30 My of simulation time. During this time, about 50 km of unstable lithospheric material is removed, thinning the thermal thickness plate by an equal amount. This indicates that the temperature structure, predicted by the half-space cooling model for plates older than 65 My, is extremely unstable in a convecting mantle, characterised by the present physical parameters.

At the base of the lithosphere, temperature increases by about 200 K with respect to predictions from the half-space cooling model (see Figure 3b). At depths between 200 and 400 km, the temperature variation is $< \pm 25$ K with respect to the initial 'adiabatic' profile, but this difference increases to > 75 K (i.e. colder) in the transition zone. However, the latter value needs to be taken with caution, since our energy equation does not include the effect of latent heat of phase transformations (olivine-wadsleyite and wadsleyite-ringwoodite). It has been shown that the temperature increase across the transition zone along an adiabat can be as much as 100 K [29]. Therefore, if we take into account this effect, the temperature difference between our initial 'adiabatic' and the final profiles is reduced to $\lesssim$ 10–20 K. This supports our choice for the temperature at the bottom of the simulation box.

3.2. *Influence of key physical parameters*

Effect of shear heating and radiogenic heat production. In the following set of numerical experiments, the effects of shear heating and radioactive heat production (RHP) are tested for a model with identical rheological parameters, as in the previous section. Table 6 lists the models and whether they include (or not) shear heating and RHP. The adopted RHP rate per unit mass is at the high end of estimated values for the mantle [21,51]. Model 09 was described in the previous section and is shown in Figure 2. We note that SSC is active in all four models.

In order to make a meaningful comparison between our results and those from conductive plate models, we calculate the averaged depth of the 1603 K isotherm by applying a moving-average filter to the depths of the isotherm. Since the wavelength of SSC is 150–200 km, a window size of 250 km removes the intrinsic local variability caused by SSC without adding significant diffusion.

Table 6. Models.

Model	SH	RHP ($W\,m^{-3}$)
09	no	0
14	yes	0
15	no	2.0×10^{-8}
16	yes	2.0×10^{-8}

The averaged 1603 K isotherm, defining the bottom of the lithosphere, for the four models is shown in Figure 4. We find that values of shear heating associated with SSC are of the same order as the RHP (10^{-8} W m^{-3}), although some punctual values can become one order of magnitude greater. Nevertheless, as shown in Figure 4 the shear heating has little influence on the final lithospheric thickness. This is because the mean shear heating remains much lower (~10–15%) than the RHP. The strain rate, and consequently the shear heating, may be underestimated in the sublithospheric mantle where the SSC cells develop. Thermally controlled shear zones may have a spatial length-scale of about 1 km [52], while the size of the elements in our model is several times greater. Nonetheless, reducing the spatial discretisation will not drastically change the viscous dissipated heat. Models 09 and 14 exhibit an average lithospheric thickness of ~200 km in plates 100 My old. This value is well outside the ranges of all existing plate models (cf. [1]), and predicts patterns of seafloor topographies and SHF that do not fit observed data satisfactory (Figure 5). On the other hand, the inclusion of RHP brings the average thickness of old oceanic lithosphere to values around 125 km, closer to results from theoretical plate models [3,53] and combined geophysical-petrological models [28]. This was also found by Huang and Zhong [12].

Influence of adiabatic heating. In the absence of other sources of heat, a fluid element would undergo changes in temperature due to variations in pressure. In a convecting mantle, major changes in pressure are related to vertical motion of material. Without adiabatic heating, the density difference between downwellings and upwellings increases, enhancing SSC. We illustrate this by setting to zero the adiabatic heating term in one of our previous models (model 95 in Figure 4). In this case, the vigour and eroding capacity of the convective cells is dramatically increased. Average lithospheric thicknesses are now 25 to 50 km thinner than in the case with adiabatic heating. As a result, seafloor topography and SHF data are more closely reproduced, although a continuous decrease with time is still seen in both observables (i.e. no flattening, Figure 5).

Adiabatic heating has been neglected in most studies addressing SSC (e.g. [11,13,14, 16,54]). Huang and Zhong [12] state that adiabatic and shear heating was explicitly included in their calculations, but no assessments of their influence on SSC or on the thermal structure of the plate were provided. Our results indicate that adiabatic heating

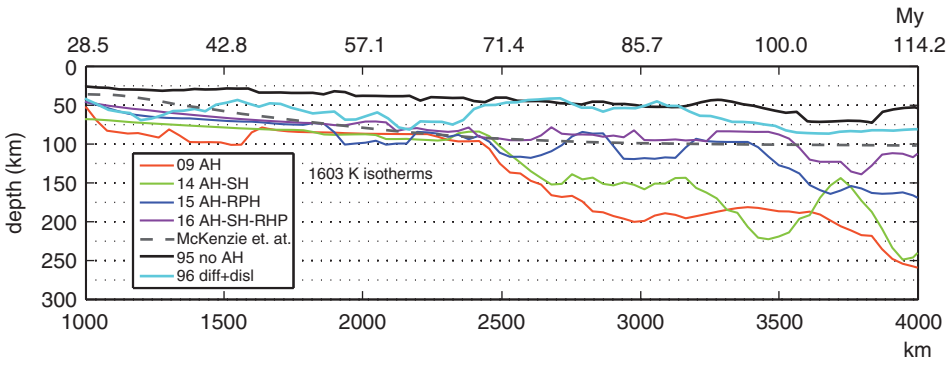

Figure 4. (Colour online). Lithospheric base defined by the averaged 1603 K isotherm.

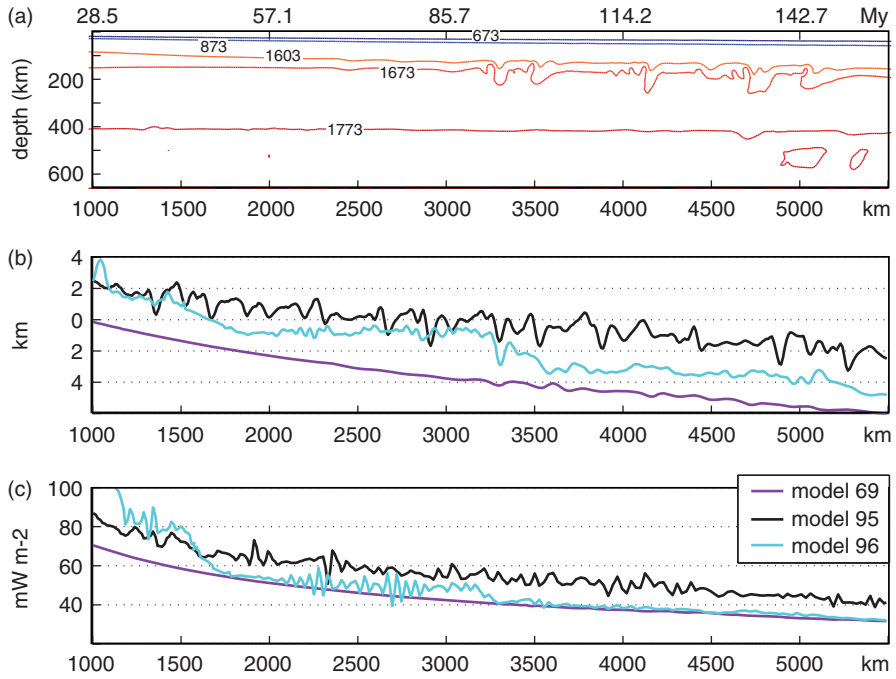

Figure 5. (Colour online). (a) Temperature in K, (b) seafloor topography, and (c) surface heat flow. Temperature in panel (a) corresponds to model 69 after 120 My of simulation time. Horizontal distance [km] is measured from the ridge, and the equivalent plate age [My] is included at the top.

exerts a major control on the final structure of the oceanic lithosphere (Figure 4). Consequently, any attempt to explain its thermal structure and associated geophysical observables using thermo-mechanical models should consider this effect. In principle, this conclusion also applies to other gravitational instabilities such as lithospheric delamination and unroofing, although further studies are needed. In this context, we emphasise that it is widely accepted that the temperature increase within most of the Earth's mantle closely follows the condition of uniform entropy (i.e. adiabatic profile, cf. [1]).

Influence of plate motion. A positive relation between the onset time of SSC and plate velocity has been reported in several studies [11,14,55]. Using isoviscous convection models, Houseman [55] found a clear delay in the SSC onset when increasing plate velocity. This author suggested that sufficiently high plate motions may even prohibit the development of gravitational instabilities. van Hunen et al. [11] described a similar behaviour in their 2D Newtonian simulations. On the other hand, Dumoulin et al. [16] found no significant correlation between the onset time of the first dripping instability and plate velocity.

We have run five Newtonian models to test the role of plate velocity on the development of SSC. The parameters used in these models are those of model 16 in Table 6. We found a positive correlation between plate velocity and SSC onset time. For velocities of 2, 4, 6, 8, and 10 cm yr^{-1}, the first drippings appear when the plate is 28, 43, 70, 72, and 80 My old, respectively, in agreement with the observations reported in [11] and [55].

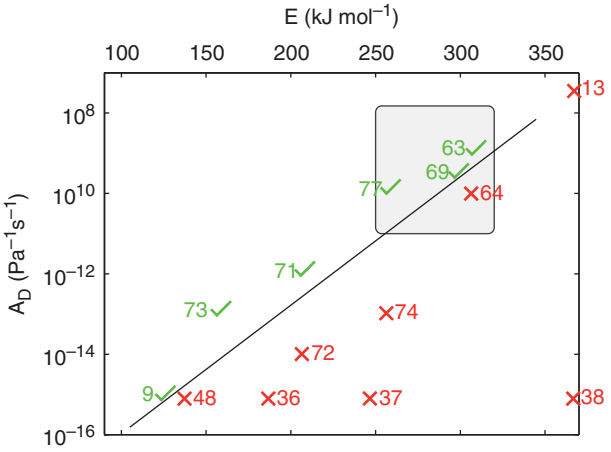

Figure 6. (Colour online). Models varying the activation energy E and the material parameter A_D. Models marked with crosses do not initiate SSC, models marked with tildes do initiate SSC. A linear relation between E and A_D defines the region where SSC is active. The grey region indicates ranges in agreement with laboratory experiments. Numbers at the side of the markers are the run number.

Influence of rheological parameters. We ran fourteen Newtonian models varying the pre-exponential factor A_D and the activation energy E to test the sensitivity of SSC to these parameters. Figure 6 shows which models developed vigorous SSC (ticks, green online) and which ones failed to do so (crosses, red online). The results suggest a quasi-linear relation between E and A_D that defines the region where SSC can be active. Moreover, the range of values that define this boundary seems to be rather limited (see, e.g. experiments 69–64 and 9–48), indicating that the development of SSC is extremely sensitive to these parameters, and hence to viscosity. In fact, the straight line in Figure 6 separates the models with average upper mantle viscosities $\lesssim$(ticks, green online) and $>$(crosses, red online) 10^{20} Pa s. The latter value is found to be a limit, above which vigorous SSC cannot develop. When the average viscosity of the upper mantle is above this threshold, the cooling of the oceanic lithosphere follows closely the HSC model. Although some small instabilities may develop at the base of the lithosphere, they cannot evolve into well defined drippings due to the high viscosity of the mantle below. This in turn precludes any significant thermal erosion of the lithosphere. A similar result was also found by [14]. On the other hand, if the average viscosity of the upper mantle is below $\sim 2 \times 10^{19}$ Pa s, velocities associated with SSC reach unrealistic values (>10 m yr^{-1}), the lithosphere is strongly eroded, and observables depart significantly from the expected values.

The shaded box in Figure 6 represents the range of values for E and A_D from laboratory experiments [21,23,26]. Three of our models (labeled as 63, 69, and 73) that developed SSC are well within this range, although their vigour is moderate. Note also that the parameters used in our previous Newtonian examples (taken from previous studies) are far from experimental results. In particular, a low value for E is commonly applied to mimic the contribution of dislocation creep [11–14], which otherwise would underestimate the erosion of the lithosphere by SSC. We anticipate, however, that the water content of residual peridotites in oceanic lithosphere, as well as their intrinsic

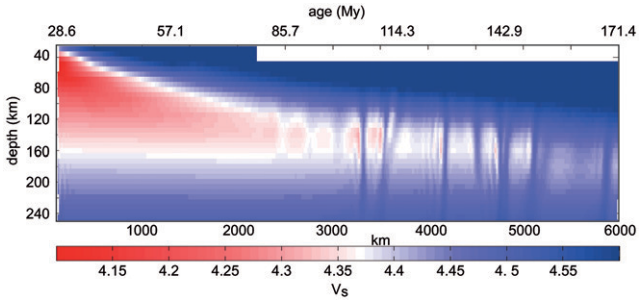

Figure 7. (Colour online). Synthetic vs. seismic structure from model 69.

compositional buoyancy, may be more important in controlling the thermal erosion of the lithosphere. A detailed assessment of these two effects is under way and will be published elsewhere.

Figure 5 shows the observables predicted by model 69. In this model, both elevation and SHF increase monotonically with age, in contrast to what is observed. However, its seismic structure (Figure 7) closely resembles those recently obtained from tomography studies in the Pacific as well as in other oceans (compare with Figure 10 in [56] and Figure 11 in [57]). Other similar models (not shown here) give identical results. This discrepancy between what is inferred from seismic data and from other observables (i.e. SHF, bathymetry) is a fundamental, yet not solved, problem in geodynamics.

4. Discussion

It is worth noting that van Hunen et al. [13] recently concluded that dislocation creep (i.e. non-Newtonian rheology) is the main deformation mechanism in the upper mantle, based on a comparison between their numerical simulations and the tomography of Ritzwoller [57] in the Pacific. The lithospheric thermal structure derived by Ritzwoller [57] shows a distinctive flattening of the isotherms (strictly, isovelocity contour lines) between 70 and 100 My, which these authors associate with a period of lithospheric reheating. van Hunen et al. [13] showed that this reheating could be modelled only with non-Newtonian models, if the adopted rheological parameters are taken to be consistent with laboratory experiments. However, the unrealistic thermal structure used in the numerical simulations (see their Figure 3), as well as the neglect of activation volumes and internal heating, make their conclusions ambiguous. Moreover, Maggi et al. [56] have recently presented a tomography for the Pacific in which no flattening of the isovelocity contour is observed. These authors pointed out that the flattening observed by Ritzwoller [57] may be an artifact, due to insufficient path coverage. If this is true, and in light of our results with Newtonian models, the argument used by van Hunen et al. [13] to favour dislocation over diffusion creep in the upper mantle becomes invalid.

There is, however, abundant independent evidence that points to dislocation creep as the main deformation mechanism in the upper mantle [21,23,26]. We have run experiments with combined dislocation-diffusion creep rheologies, always restricting rheological parameters to realistic ranges (i.e. within the shaded box in Figure 6 for

diffusion creep, and $n = 3.5$, $E = 500$, $V = 17$ and $A_D = 2.42 \times 10^{-14}$ for dislocation creep), to test the potential eroding effect of dislocation creep. In our simulations, dislocation creep becomes dominant in the first 250–300 km (i.e. $\eta_{disl} < \eta_{diff}$) and generates an extra 20–50 km of erosion at the bottom of the lithosphere (Figure 4). Due to the greater activation volume of dislocation creep, and the small convective stresses generated below ~250 km depth ($\lesssim$0.1 MPa), diffusion creep becomes dominant below this depth. Interestingly, the resulting seafloor topography and SHF exhibit wide regions where the signals become flat (Figure 5), but the overall fitting to observed data is still poor.

In a recent study, Korenaga and Korenaga [58] argued that the 'normal' evolution of seafloor topography may be explained by the half-space cooling models. These authors conclude that most of the observed bathymetric signal is influenced by anomalous crust and hot-spots, and therefore, they do not necessarily reflect the normal evolution of the oceanic lithosphere. This conclusion is in agreement with the seismic tomography of [56] and the results reported in this study. If true, it could offer (at least partially) a solution to the mentioned dichotomy between surface observables and seismic observations.

As a final caveat, we note that our 2D results may represent lower bounds in terms of SSC vigour and eroding capacity. Results from 3D numerical [11] and laboratory experiments on SSC [59,60] indicate that longitudinal rolls (LR; aligned with plate motion) tend to be favoured over transverse rolls (TR; perpendicular to plate motion). More importantly, there is evidence that LR are more vigorous than TR, and that plate motion enhances SSC in 3D models, contrary to what is predicted by 2D simulations [11]. If these observations are correct, 3D SSC could lead to thinner plates than those obtained in 2D simulations, at least for fast-moving plates. Whether or not this would result in a significant modification of the thermal structure of plates or in a better fitting of the observables remains to be tested.

Further studies on (i) the viscosity structure of the oceanic upper mantle, (ii) the influence of shallow phase changes and melt dehydration on SSC, and (iii) high-resolution seismic experiments will provide crucial insights into the evolution of the oceanic lithosphere.

5. Conclusions

We have studied the development and evolution of small-scale gravitational instabilities under the Earth's oceanic lithosphere using numerical simulations. Our results can be summarised as follow:

(i) The influence of three different heating terms was tested. Shear heating has negligible influence on the overall temperature of the model as well as on SSC. In contrast, heat from radiogenic sources increases mantle temperatures, favours the development of SSC, and reduces the average thermal thickness of the lithosphere. The inclusion of adiabatic heating reduces the temperature contrasts between ambient mantle and downwellings/upwellings. This in turn diminishes the vigour of SSC and lithospheric erosion.

(ii) A low viscosity region below the lithosphere is needed to develop and maintain SSC. The height of this zone has to be similar to the horizontal wavelength of instabilities ($\geq$200 km). For realistic rheological parameters, the average viscosity in this region cannot be higher than $\sim 10^{20}$ Pa s.

(iii) Small-scale convection can be generated using experimentally derived rheological parameters cells. Nevertheless, the activation of SSC does not always result in significant lithospheric erosion. To reduce the lithospheric thickness considerably, Newtonian models need activation energy and pre-exponential factor values that are too low in comparison with those reported in laboratory studies. In models where both deformation mechanisms (i.e. diffusion and dislocation) are present, the low viscosity zone is dominated by dislocation and considerable lithospheric erosion occurs.

(iv) A positive relation is observed between plate velocity and SSC onset time. This corroborates results from previous studies.

(v) Although our synthetic seismic structures closely resemble results from tomography studies in oceanic mantle, seafloor topography and SHF hardly fit the observed trends in old lithospheres. Further numerical and seismological studies are needed to explain this discrepancy.

Acknowledgements

We thank the organisers of the IAS workshop B. Sluys, A. Suiker, H. Mühlhaus, E. Busso, and A. Benallal for the invitation to contribute to this special volume. Constructive reviews from K. Regenauer-Lieb and an anonymous reviewer are gratefully acknowledged. This research has been supported by the Spanish Team Consolider-Ingenio 2010 nrCSD2006-00041.

References

[1] G. Schubert, D.L. Turcotte and P. Olson, *Mantle Convection in Earth and Planets*, Cambridge University Press, Cambridge, 2001.
[2] D.P. McKenzie, J. Geophys. Res. 72 (1967) p.6261.
[3] B. Parsons and J.G. Sclater, J. Geophys. Res. 82 (1977) p.803.
[4] D.L. Turcotte and E.R. Oxburgh, J. Fluid Mech. 28 (1967) p.29.
[5] W. Schroeder, J. Geophys. Res. 89 (1984) p.9873.
[6] C.A. Stein and S. Stein, Nature 129 (1992) p.123.
[7] B. Parsons and D. McKenzie, J. Geophys. Res. 83 (1978) p.4485.
[8] D.A. Yuen, W.R. Peltier and G. Schubert, Geophys. J. Roy. Astron. Soc. 65 (1981) p.171.
[9] C. Jaupart and B. Parsons, Phys. Earth Planet. Inter. 39 (1985) p.14.
[10] D.A. Yuen and L. Fleitout, Nature 313 (1985) p.125.
[11] J. van Hunen, J. Huang and S. Zhong, Geophys. Res. Lett. 30, doi:10.1029/2003GL018101 (2003).
[12] J. Huang and S. Zhong, J. Geophys. Res. 110, doi:10.1029/2004JB003153 (2005).
[13] J. van Hunen, S. Zhong, N.M. Shapiro et al., Earth Planet. Sci. Lett. 238 (2005) p.146.
[14] J. Huang, S. Zhong and J. van Hunen, J. Geophys. Res. 108, doi:10.1029/2003JB002456 (2003).
[15] J. Korenaga and T.H. Jordan, J. Geophys. Res. 109, doi:10.1029/2003JB002464 (2004).
[16] C. Dumoulin, M.P. Doin and L. Fleitout, Phys. Earth Planet. Int. 125 (2001) p.45.
[17] N.W.E. Curlet, Phys. Earth Planet. Int. 125 (2001) p.45.
[18] F.H. Busse, *Mantle convection. Plate tectonics and global dynamics*, in *The Fluid Mechanics of Astrophysics and Geophysics*, W.R. Peltier ed., Gordon and Breach Science Publishers, Montreux, 1989, pp.23–95.
[19] J. Donea and A. Huerta, *Finite Element Methods for Flow Problems*, John Wiley, Chichester, 2002.

[20] S. Zlotnik, P. Díez, M. Fernández et al., Comput. Methods Appl. Mech. Eng. 196 (2007) p.4283.
[21] G. Ranalli, *Rheology of the Earth*, 2nd ed., Chapman and Hall, London, 1995.
[22] S.H. Kirby, Rev. Geophys. 21 (1983) p.1458.
[23] G. Hirth and D. Kohlstedt, *Rheology of the upper mantle and the mantle wedge: A view from the experimentalists*, in *Inside the Subduction Factory, AGU Geophys. Monograph Series*, Vol. 138, J. Eiler ed., AGU, Washington DC, 2004, p.138.
[24] M. Nettles and A.M. Dziewonski, J. Geophys. Res. 113 (2008).
[25] D. Mainprice, A. Tommasi, H. Couvy et al., Nature 433 (2005) p.731.
[26] S.-I. Karato and P. Wu, Rev. Science 260 (1993) p.771.
[27] K. Regenauer-Lieb, B. Hobbs, D.A. Yuen et al., Phil. Mag. 86 (2006) p.3373.
[28] J.C. Afonso, G. Ranalli and M. Fernàndez, Geophys. Res. Lett. 34, doi:10.1029/2007GL029515 (2007) p.L10302.
[29] T. Katsura, H. Yamada, O. Nishikawa et al., J. Geophys. Res. 109, doi:10.1029/2003JB002438 (2004).
[30] A. Guest, G. Schubert and C.W. Gable, Phys. Earth Planet. Inter. 149 (2004) p.187.
[31] T. Katsura and E. Ito, J. Geophys. Res. 94 (1989) p.15663.
[32] L. Stixrude and C. Lithgow-Bertelloni, Earth Planet. Sci. Lett. 263 (2007) p.45.
[33] L. Stixrude and C. Lithgow-Bertelloni, J. Geophys. Res. 110, doi:10.1029/2004JB002965 (2005) p.B03204.
[34] D.L. Schutt and C.E. Lesher, J. Geophys. Res. 111, doi:10.1029/2003JB002950 (2006).
[35] M.E. Akaogi, E. Ito and A. Navrotsky, J. Geophys. Res. 94 (1989) p.15671.
[36] Y. Fei, *Thermal expansion*, in *Mineral Physics and Crystallography, A Handbook of Physical Contents*, T. Ahren ed., AGU, Washington DC, 1995, pp.29–44.
[37] A.R. Oganov, J.P. Brodholt and G.D. Price, Earth Planet. Sci. Lett. 184 (2001) p.555.
[38] A. Chopelas, Am. Miner. 85 (2000) p.270.
[39] J.C. Afonso, G. Ranalli and M. Fernández, Phys. Earth Planet. Inter. 149 (2005) p.279.
[40] A.M. Hofmeister, Science 283 (1999) p.1969.
[41] J.C. Afonso, M. Fernàndez, G. Ranalli et al., Geochem. Geophys. Geosyst. 9 (2008).
[42] G.T. Jarvis and W.R. Peltier, Geophys. J. R. Astron. Soc. 68 (1982) p.389.
[43] D.P. McKenzie, Geophys. J. Roy. Astron. Soc. 48 (1977) p.211.
[44] G. Marquart and H. Schmeling, Geophys. J. 97 (1989) p.511.
[45] J.A.D. Connolly, Earth Planet. Sci. Lett. 236 (2005) p.524.
[46] S.I. Karato, Geophys. Res. Lett. 20 (1993) p.1623.
[47] I. Jackson, J.D. FitzGerald, U.H. Faul et al., J Geophys. Res. 107, NO.B12,1360, doi:10.1029/2001JB001225 (2002).
[48] U.H. Faul and I. Jackson, Earth Planet. Sci. Lett. 234 (2005) p.119.
[49] A.E. Gripp and R.G. Gordon, Geophys. J. Int. 150 (2002) p.321.
[50] J. Korenaga, Geophys. Res. Lett. 29, doi:10.1029/2002GL016085 (2002).
[51] S. Labrosse and C. Jaupart, Earth Planet. Sci. Lett. 260 (2007) p.465.
[52] K. Regenauer-Lieb and D.A. Yuen, Earth Sci. Rev. 63 (2003) p.295.
[53] D. McKenzie, J. Jakson and K. Priestely, Earth Planet. Sci. Lett. 233 (2005) p.337.
[54] S.E. Zaranek and E.M. Parmentier, J. Geophys. Res. 109, doi:10.1029/2003JB002462 (2004).
[55] G. Houseman, Geophys. J. R. Astron. Soc. 75 (1983) p.309.
[56] A. Maggi, E. Debayle, K. Priestly et al., Geophys. J. Int. 166 (2006) p.1384.
[57] M. Ritzwoller, N. Shapiro and S.-J. Zhong, Earth Planet. Sci. Lett. 226 (2004) p.69.
[58] T. Korenaga and J. Korenaga, Earth Planet. Sci. Lett. 268, doi: 10.1016/j.epsl.2007.12.022 (2008).
[59] F.M. Richter, J. Geophys. Res. 78 (1973) p.8735.
[60] F.M. Richter and B. Parsons, J. Geophys. Res. 80 (1975) p.2529.